Matrix-Free Method for Transient Maxwell-Thermal Cosimulation in Arbitrary Unstructured Meshes

Kaiyuan Zeng, *Graduate Student Member, IEEE*, and Dan Jiao, *Fellow, IEEE*

***Abstract*— Existing electrical–thermal cosimulation methods require solving a system matrix when handling inhomogeneous materials and irregular geometries discretized into unstructured meshes. In this paper, a matrix-free method is developed for cosimulating full-wave Maxwell's equations and the thermal diffusion equation in the time domain. The method is free of matrix solutions regardless of the shape of the element used for space discretization. A theoretical stability analysis is also developed for the coupled electrical and thermal analysis, which is nonlinear in nature. Numerical experiments on both unstructured tetrahedral and triangular prism element meshes have validated the accuracy and efficiency of the proposed method.**

***Index Terms*— Electrical–thermal cosimulation, matrix-free methods, multiphysics simulation, thermal analysis, time-domain methods.**

I. Introduction

THE analysis of a multiphysics problem involves the solution of multiple partial differential equations (PDEs). Existing solvers for solving PDEs generally cast the original physical problem into a matrix equation of $\mathbf{A}x = b$ to solve [1], [2], where $\mathbf{A}$ can be either dense or sparse. The solution of such a matrix equation can be computationally expensive, i.e., requiring prohibitively large memory and/or long CPU runtime, in unstructured meshes, as system matrix $\mathbf{A}$ is, in general, not diagonal. If a numerical method for solving PDEs can be made matrix-free, i.e., free of a matrix solution, then much larger problems can be solved using the same computational resources.

The finite-difference time-domain (FDTD) method [3], [4] has its merit in being simple and free of a system matrix solution. However, it has been difficult to extend the FDTD to arbitrary unstructured meshes [5]. Nonorthogonal FDTD methods [6]–[11] generally require a dual mesh, which is not straightforward to construct for a primary mesh that must capture arbitrarily shaped material discontinuities in 3-D settings. Interpolations and projections are often employed in these methods, and stability and accuracy may not be simultaneously guaranteed. Recently, a matrix-free time-domain method has been developed for solving Maxwell's PDE equations in unstructured meshes [12]–[14]. This method has a naturally diagonal system matrix independent of the element shape used for discretization, and hence, the need for numerically finding the matrix solution is completely eliminated. Despite the success of solving Maxwell's equations, however, a matrix-free time-domain method has not been developed for thermal analysis as well as electrical–thermal codesign and analysis. In the existing methods for thermal simulation and electrical–thermal cosimulation [15]–[22], based on either static or full-wave Maxwell's equations, a matrix solution is required when dealing with unstructured meshes. These meshes are often necessary for discretizing irregularly shaped geometries and materials. They also help greatly reduce the number of unknowns as compared with a grid-based discretization. Since the material property changes with time due to thermal effects, the system matrix resulting from the discretization of Maxwell's equations is time-dependent in an electrical–thermal cosimulation. As a result, at each time instant when the matrix changes, one has to refactorize or solve the matrix, which is time-consuming, especially in analyzing large-scale problems. Although the matrix-free time-domain method [12] has a flexible framework, it cannot be directly applied to perform a thermal analysis, since it is formulated for vectors while the thermal diffusion equation is a scalar equation. In addition, the cosimulation of the coupled Maxwell's and thermal equations results in a nonlinear system of equations, the stability of which has not been investigated in the existing methods.

The electrical–thermal coanalysis is of critical importance in advanced integrated circuit (IC) design, where emerging interconnect solutions have been intensively pursued to overcome the shortcoming of existing copper-based interconnects in performance and reliability. The design of the new interconnect solutions typically involves many physics, such as circuits, electromagnetics, materials, electron transport, and thermal diffusion in a broadband of frequencies. To understand the entire physical process happening in an advanced IC design, a rigorous and efficient multiphysics simulation is required.

In view of the importance of the electrical–thermal coanalysis and the shortcoming of the existing methods, in this paper, we develop a matrix-free algorithm for solving full-wave Maxwell's equations and the thermal diffusion equation simultaneously. The proposed new algorithm is made naturally free of matrix solutions. Hence, it has a potential of being much more efficient in time and memory than solvers requiring solving matrices. The matrix-free property of the proposed

Manuscript received May 2, 2018; revised August 17, 2018; accepted August 30, 2018. Date of publication October 30, 2018; date of current version December 11, 2018. This work was supported in part by a grant from the National Science Foundation under Award 1619062 and in part by a grant from DARPA under Award FA8650-18-2-7847. This paper is an expanded version from the IEEE MTT-S International Microwave Symposium (IMS2018), Philadelphia, PA, USA, June 10–15, 2018. *(Corresponding author: Dan Jiao.)*

The authors are with the School of Electrical and Computer Engineering, Purdue University, West Lafayette, IN 47907 USA (e-mail: djiao@purdue.edu).

Color versions of one or more of the figures in this paper are available online at http://ieeexplore.ieee.org.

Digital Object Identifier 10.1109/TMTT.2018.2875105

method is achieved regardless of the element shape used for discretization, thus suitable for both regular grid-based discretizations and unstructured meshes. The basic idea of this paper has been presented in [23], while this paper completes [23] from the perspectives of both algorithm development and numerical experiments. The stability of the coupled nonlinear system of equations is also analyzed in detail and found to be ensured with a correct choice of time step in explicit time marching. In [12]–[14], we develop the matrix-free method for solving Maxwell's equations only. These papers do not address the thermal analysis as well as the combined electrical–thermal analysis concerned in this paper. Numerical experiments have validated the accuracy and efficiency of the proposed method.

II. Equations Governing Electrical–Thermal Cosimulation

The electrical performance of a physical structure is governed by the Maxwell's equations from dc to high frequencies [12]

$$\nabla \times \mathbf{E} = -\mu \frac{\partial \mathbf{H}}{\partial t} \tag{1}$$

$$\nabla \times \mathbf{H} = \epsilon \frac{\partial \mathbf{E}}{\partial t} + \sigma \mathbf{E} + \mathbf{J} \tag{2}$$

where $\mathbf{E}$ is the electric field intensity, $\mathbf{H}$ is the magnetic field intensity, $\mathbf{J}$ is the input (supply) current density, and μ, ϵ, and σ are the permeability, permittivity, and conductivity, respectively.

The thermal performance is dictated by the well-known thermal diffusion equation [15]

$$\tilde{\rho} c_p \frac{\partial T}{\partial t} - \nabla \cdot (k \nabla T) = P_{\text{joule}} + P_0 \tag{3}$$

where k is the thermal conductivity, c_p is the specific heat capacity, $\tilde{\rho}$ denotes the mass density of the material, T is the temperature, P_{joule} represents the heat source

$$P_{\text{joule}} = \mathbf{J} \cdot \mathbf{E} = \sigma E^2 \tag{4}$$

and P_0 denotes other heat sources. The conductivity is a function of temperature, which obeys

$$\sigma = \frac{\sigma_0}{1 + \alpha (T - T_0)} \tag{5}$$

in which σ_0 is the conductivity at temperature T_0 and α is the temperature coefficient of the material.

Equations (1)–(5) can be cosimulated as follows to obtain the electrical and thermal performance of a structure. Starting from an initial temperature, and hence an initial conductivity of the material, (1) and (2) can be solved to find electric field distribution in the entire structure. This will provide a heat source P_{joule} to (3). Equation (3) can then be simulated to find the temperature distribution. The temperature distribution is subsequently used to update the conductivity of the material through (5). Equations (1) and (2) are then simulated again with the updated σ value. The entire simulation repeats until the desired time or a steady state is reached.

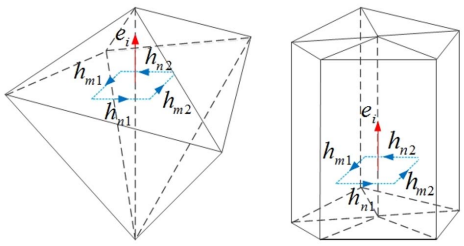

Fig. 1. Choice of **H**-points and directions.

III. Proposed Work

In this section, we present a matrix-solution free method for solving the coupled electrical–thermal equations.

A. Matrix-Free Time-Domain Method for Solving Maxwell's Equations

Consider a physical structure discretized into either a regular grid or an unstructured mesh consisting of arbitrarily shaped elements. Based on [12], to discretize Faraday's law, we expand the electric field $\mathbf{E}$ in each element by vector bases, yielding $\mathbf{E} = \sum_{j=1}^{m} u_j \mathbf{N}_j$, where u_j is the jth basis's unknown coefficient and m is the basis number in each element. The first-order vector bases are used as $\mathbf{N}_j$, such that they can produce the second-order accurate magnetic fields anywhere to facilitate an accurate discretization of Ampere's law (2). Substituting the expansion of $\mathbf{E}$ into Faraday's law (1), evaluating $\mathbf{H}$ at the point individuated by the distance vector $\mathbf{r}_{hi}$, and then taking the dot product of the resultant with unit vector $\hat{h}_i$, we obtain

$$\mathbf{S}_e\{u\} = -\text{diag}(\{\mu\}) \frac{\partial \{h\}}{\partial t} \tag{6}$$

where u denotes a global $\mathbf{E}$-unknown vector of length N_e consisting of all u_j coefficients and $\mathbf{S}_e$ is a sparse matrix whose ijth entry is

$$\mathbf{S}_{e,ij} = \hat{h}_i \cdot \{\nabla \times \mathbf{N}_j\}(\mathbf{r}_{hi}) \tag{7}$$

and h is a global H-unknown vector of length N_h, whose ith entry is $h_i = \mathbf{H}(\mathbf{r}_{hi}) \cdot \hat{h}_i$. The number of nonzero elements in each row of $\mathbf{S}_e$ is the number of basis functions in each element, which is a small constant; diag($\{\mu\}$) in (6) is a diagonal matrix of magnetic permeability μ. The **H**-points and directions are chosen along a rectangular loop perpendicular to each E-unknown, and centering the E-unknown, as shown in Fig. 1. In this way, the resultant H-fields can, in turn, generate desired E accurately. Unlike the FDTD method, here, the **H**-points and directions do not form a dual mesh. Only a single mesh is needed. No interpolations and projections are required either.

To discretize Ampere's law, we apply the law at $\mathbf{r}_{ei}$ points and then take the dot product of the resultant with unit vector $\hat{e}_i$ at each point, obtaining

$$\mathbf{S}_h\{h\} = \text{diag}(\{\epsilon\}) \frac{\partial \{e\}}{\partial t} + \text{diag}(\{\sigma\})\{e\} + \{j\} \tag{8}$$

in which $\mathbf{S}_h$ is a sparse matrix of size $N_e \times N_h$. Each row of $\mathbf{S}_h$ has only four nonzero elements, whose column index corresponds to the global index of the four H-points associated with one E-unknown. In (8), diag($\{\epsilon\}$) and diag($\{\sigma\}$) are the diagonal matrices of permittivity and conductivity, respectively.

With $\{u\} = \{e\}$, (6) and (8) are connected, and they can be solved in a leapfrog way, which is free of matrix solutions [3]. We can also eliminate $\mathbf{H}$ and solve $\mathbf{E}$ as follows:

$$\frac{\partial^2\{e\}}{\partial t^2} + \text{diag}\left(\left\{\frac{1}{\epsilon}\right\}\right)\frac{\partial\{\sigma e\}}{\partial t} + \mathbf{S}\{e\} = -\text{diag}\left(\left\{\frac{1}{\epsilon}\right\}\right)\frac{\partial\{j\}}{\partial t} \tag{9}$$

where

$$\mathbf{S} = \text{diag}\left(\left\{\frac{1}{\epsilon}\right\}\right)\mathbf{S}_h\text{diag}\left(\left\{\frac{1}{\mu}\right\}\right)\mathbf{S}_e. \tag{10}$$

In (9), σ is not taken out of the time derivative because it is time-dependent in an electrical–thermal cosimulation. Obviously, the matrices in front of both the second- and first-order time derivatives in (9) are diagonal. Therefore, an explicit marching of (9), such as a central-difference-based time marching [1], is free of matrix solutions.

B. Matrix-Free Time-Domain Method for Solving Thermal Diffusion Equation

Although the thermal diffusion equation is a scalar equation, its matrix-free solution in unstructured meshes does not exist in the open literature. Using the finite-element method or other PDE methods, the resultant numerical system involves a sparse matrix to solve. To develop a matrix-free solution of (3), we propose to first vectorize the scalar-based (3). Although this approach appears to complicate the problem to be solved, the end result is efficient as the number of temperature unknowns to solve remains the same as before.

We append a direction to T, making it a vector $\mathbf{T}$. For example, in (3), if we attach a unit vector along z to the right-hand side heat source $P_{\text{joule}} + P_0$, then the $\mathbf{T}$'s z-component solved from a vector-based (3) would be the real temperature. To develop a matrix-free solution of (3), we also introduce an auxiliary vector $\mathbf{T}_c$, which corresponds to the curl of the $\mathbf{T}$ vector. With the two vector variables, we transform the original thermal diffusion equation (3) into the following two vector equations to solve:

$$k\nabla \times \mathbf{T} = -\frac{\partial \mathbf{T}_c}{\partial t} \tag{11}$$

$$\nabla \times \mathbf{T}_c = \tilde{\rho} c_p \mathbf{T} - \int (\mathbf{P}_{\text{joule}} + \mathbf{P}_0)\text{d}t. \tag{12}$$

Next, we show the equivalency between (3) and the above-discussed two equations. Consider a source-free region with uniform thermal constants for convenience. Starting from (11) and (12), we have

$$\tilde{\rho} c_p \nabla \cdot \mathbf{T} = \nabla \cdot (\nabla \times \mathbf{T}_c) = 0. \tag{13}$$

Using the curl of the curl property [24], we obtain

$$\nabla \times \nabla \times \mathbf{T} = \nabla(\nabla \cdot \mathbf{T}) - \nabla^2 \mathbf{T} = -\nabla^2 \mathbf{T}. \tag{14}$$

By taking a curl of (11) and substituting (12) into the resultant, we have

$$\tilde{\rho} c_p \frac{\partial \mathbf{T}}{\partial t} + k\nabla \times \nabla \times \mathbf{T} = \mathbf{P}_{\text{joule}} + \mathbf{P}_0. \tag{15}$$

The above-mentioned equation is the same as (3) by utilizing the relationship of (14). As a result, solving the two vector equations (11) and (12) simultaneously is equivalent to solving (3).

Obviously, (11) has the same form as Faraday's law, while (12) has a form similar to Ampere's law. Hence, the matrix-free time-domain method can be applied to solve (11) and (12) without any need for solving a matrix equation. First, we can expand $\mathbf{T}_c$ using a set of first-order vector bases and then evaluate (12) at $\mathbf{r}_{ti}$ along direction $\hat{h}_{ti}$ ($i = 1, 2, \ldots, N_t$). Therefore, (12) can be discretized as

$$\mathbf{S}_e\{T_c\} = \text{diag}(\{\tilde{\rho} c_p\})\{T\} - \{P\} \tag{16}$$

where $\{P\}$ denotes the vector associated with heat source's time integration. On the other hand, we can discretize (11) as

$$\text{diag}(\{k\})\mathbf{S}_h\{T\} = -\frac{\partial\{T_c\}}{\partial t} \tag{17}$$

the accuracy of which is guaranteed by (16), since T therein is generated at the points and along the directions that ensure the second-order accuracy of (17). In (16) and (17), both $\mathbf{S}_e$ and $\mathbf{S}_h^T$ are sparse. Their sizes are $N_t \times N_c$, where N_t is the number of $\mathbf{T}$ unknowns, while N_c is the number of $\mathbf{T}_c$ unknowns. diag$\{k\}$ and diag$\{\tilde{\rho} c_p\}$ are diagonal matrices of k_i and $\tilde{\rho}_i c_{pi}$, respectively. Vector $\{T\}$ contains all the $\mathbf{T}$ unknowns, while vector $\{T_c\}$ contains all the $\mathbf{T}_c$ unknowns.

Equations (16) and (17) can be solved without any matrix solution using a forward difference scheme. We can also eliminate $\mathbf{T}$ and solve for $\mathbf{T}_c$ first as follows:

$$\frac{\partial\{T_c\}}{\partial t} + \mathbf{S}_{t_c}\{T_c\} = \{b\} \tag{18}$$

where

$$\mathbf{S}_{t_c} = \text{diag}(\{k\})\mathbf{S}_h\text{diag}\left(\left\{\frac{1}{\tilde{\rho} c_p}\right\}\right)\mathbf{S}_e \tag{19}$$

$$\{b\} = -\text{diag}(\{k\})\mathbf{S}_h\text{diag}\left(\left\{\frac{1}{\tilde{\rho} c_p}\right\}\right)\{P\} \tag{20}$$

and (18) can be discretized in time as the following:

$$\{T_c\}^{n+1} = \{T_c\}^n - \Delta t \mathbf{S}_{t_c}\{T_c\}^n + \{b\}^n. \tag{21}$$

Once $\{T_c\}$ is solved at each time step, $\{T\}$ can be obtained readily from (16). Obviously, no matrix equation needs to be solved in (21); thus, a linear (optimal) complexity is achieved in computation. Alternatively, we can also eliminate $\mathbf{T}_c$ and directly solve for $\mathbf{T}$ as follows:

$$\frac{\partial\{T\}}{\partial t} + \mathbf{S}_t\{T\} = \text{diag}\left(\left\{\frac{1}{\tilde{\rho} c_p}\right\}\right)\{P_{\text{joule}} + P_0\} \tag{22}$$

where the ith entry of $\{P_{\text{joule}} + P_0\}$ is the heat source at the ith temperature point, and

$$\mathbf{S}_t = \text{diag}\left(\left\{\frac{1}{\tilde{\rho} c_p}\right\}\right)\mathbf{S}_e\text{diag}\left(\{k\}\right)\mathbf{S}_h. \tag{23}$$

The aforementioned approach obviously is very different from prevailing methods for solving the thermal equation, where the temperature unknown is expanded into certain scalar basis functions, and then, the equation is tested also by certain basis functions. The resultant numerical system matrix is not diagonal and hence must be solved at each time step. In contrast, in the proposed matrix-free method, by introducing a vector-based representation of temperature unknown, and its curl vector, we can interleave the two unknowns in both time and space and develop an explicit time-domain solution of the thermal diffusion equation that is free of matrix solutions. Apparently, by vectorizing T, we complicate the problem. In fact, the size of the resulting numerical system for T, as shown in (22), is the same as before, which is the number of temperature unknowns in the discretized structure.

C. System for Electrical–Thermal Cosimulation and Stability Analysis

After using the proposed matrix-free time-domain method, we obtain the following system of equations for electrical–thermal cosimulation:

$$\frac{\partial^2\{e\}}{\partial t^2} + \text{diag}\left(\left\{\frac{1}{\epsilon}\right\}\right)\frac{\partial\{\sigma e\}}{\partial t} + \mathbf{S}\{e\} = -\text{diag}\left(\left\{\frac{1}{\epsilon}\right\}\right)\frac{\partial\{j\}}{\partial t} \tag{24}$$

$$\frac{\partial\{T\}}{\partial t} + \mathbf{S}_t\{T\} = \text{diag}\left(\left\{\frac{1}{\tilde{\rho}c_p}\right\}\right)\{\sigma e^2\} \tag{25}$$

$$\sigma = \frac{\sigma_0}{1+\alpha(T-T_0)} \tag{26}$$

where P_{joule} is present as the heat source. The above-discussed equations are clearly coupled. If we define a global vector of

$$x = \{e\ h\}^T \tag{27}$$

and

$$y = \{T - T_0\} \tag{28}$$

the coupled electrical–thermal system can be rewritten as

$$\begin{aligned} x'(t) &= -\begin{bmatrix}\text{diag}(\{\epsilon\}) & 0\\ 0 & \text{diag}(\{\mu\})\end{bmatrix}^{-1} \\ &\quad\times\begin{bmatrix}\text{diag}\left(\left\{\frac{\sigma_0}{1+\alpha y}\right\}\right) & -\mathbf{S}_h\\ \mathbf{S}_e & 0\end{bmatrix}x + f \\ y'(t) &= -\mathbf{S}_t y + \left[\text{diag}\left\{\frac{\sigma_0}{\tilde{\rho}c_p(1+\alpha y)}\right\}\quad 0\right]x^2 \end{aligned} \tag{29}$$

where superscript $'$ denotes a time derivative and $f = \{-j/\epsilon\ 0\}^T$ is the source term.

Equation (29) constitutes a nonlinear system of equations. The stability of a nonlinear system can be analyzed by finding its Jacobian matrix at each solution point (x_n, y_n). Take the equilibrium point as an example, this is the point (x_0, y_0) at which the right-hand side of (29) becomes zero when the source f is vanished. This point can be readily found as $x_0 = 0, y_0 = 0$. Evaluating the Jacobian matrix of (29) at (x_0, y_0), we obtain

$$\mathcal{J} = \begin{bmatrix} -\begin{bmatrix}\text{diag}(\{\sigma_0\epsilon^{-1}\}) & -\text{diag}(\{\epsilon^{-1}\})\mathbf{S}_h\\ \text{diag}(\{\mu^{-1}\})\mathbf{S}_e & 0\end{bmatrix} & 0\\ 0 & -\mathbf{S}_t\end{bmatrix}. \tag{30}$$

In a regular grid, $\mathbf{S}_t$ is positive semidefinite, as $\mathbf{S}_h = \mathbf{S}_e^T$. As for the first diagonal block in (30), its eigenvalues λ and eigenvectors v satisfy

$$-\begin{bmatrix}\text{diag}(\{\sigma_0\epsilon^{-1}\}) & -\text{diag}(\{\epsilon^{-1}\})\mathbf{S}_h\\ \text{diag}(\{\mu^{-1}\})\mathbf{S}_e & 0\end{bmatrix}\begin{bmatrix}v_1\\ v_2\end{bmatrix} = \lambda\begin{bmatrix}v_1\\ v_2\end{bmatrix}. \tag{31}$$

Substituting the second subsystem of equations of the above into the first, we obtain

$$\lambda^2 v_1 + \lambda\text{diag}\left(\left\{\frac{\sigma_0}{\epsilon}\right\}\right)v_1 + \mathbf{S}v_1 = 0 \tag{32}$$

where $\mathbf{S}$ is the same as shown in (10). In a regular gird, $\mathbf{S}$ is positive semi-definite. Since $\text{diag}(\{(\sigma_0/\epsilon)\})$ is positive semi-definite as well, the eigenvalues of (32) have a nonpositive real part. Hence, the eigenvalues of the Jacobian matrix $\mathcal{J}$ have a nonpositive real part. Therefore, based on the stability theory of a nonlinear system [25], an explicit marching of (29) is stable at (x_0, y_0).

The Jacobian matrix of (29) is time-dependent. At an arbitrary solution point (x_n, y_n), the Jacobian matrix of (29) can be written as

$$\mathcal{J}_n = \begin{bmatrix} -\begin{bmatrix}\text{diag}(\{\sigma_n\epsilon^{-1}\}) & -\text{diag}(\{\epsilon^{-1}\})\mathbf{S}_h\\ \text{diag}(\{\mu^{-1}\})\mathbf{S}_e & 0\end{bmatrix} & 0\\ 2\left[\text{diag}\left\{\frac{\sigma_n}{\tilde{\rho}c_p}\right\}\quad 0\right]x_n & -\mathbf{S}_t\end{bmatrix} \tag{33}$$

in which σ_n and x_n represent σ and x at the nth time step, respectively. Since the above-mentioned matrix is triangular, the eigenvalues are determined by the eigenvalues of the diagonal blocks. Hence, the property of the eigenvalues is the same as that of (30). Thus, an explicit time marching is stable.

From (30) and (33), it can also be seen that the Maxwell's subsystem and the thermal one are governed by different eigenvalues, with the magnitude of the latter much smaller. To see this point clearly, (29) can be split into the following two subsystems at an arbitrary nth time step:

$$x_n' = \mathcal{J}_n(1,1)x_n + f_n \tag{34}$$

$$y_n' = \mathcal{J}_n(2,2)y_n + \left[\text{diag}\left\{\frac{\sigma_n}{\tilde{\rho}c_p}\right\}\quad 0\right]x_n^2 \tag{35}$$

where the eigenvalues of $\mathcal{J}_n(1,1)$ (the first diagonal block of $\mathcal{J}_n$) are related to Maxwell's equations, and the eigenvalues of $\mathcal{J}_n(2,2) = -\mathbf{S}_t$ are solely related to the thermal equation. Hence, the choice of time step can be made different. In this paper, we employ a forward difference to discretize the thermal equation. Performing a stability analysis of the forward differencing of (35), it can be readily found that the time step should satisfy

$$\Delta t_t < \frac{2\text{Re}(\lambda_{\text{ther}})}{|\lambda_{\text{ther}}|^2} \tag{36}$$

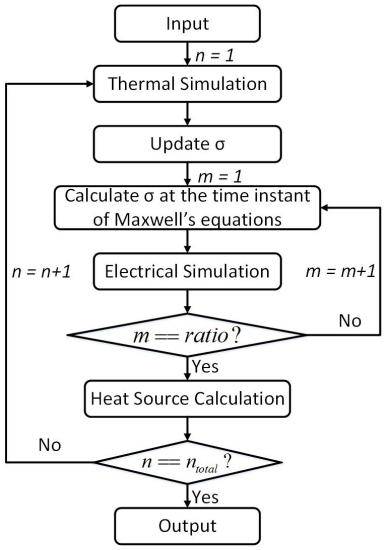

Fig. 2. Flowchart of the cosimulation algorithm.

where λ_{ther} is the eigenvalue of $\mathbf{S}_t$ whose magnitude is the largest. $|\lambda_{\text{ther}}|$ can be analytically estimated as

$$|\lambda_{\text{ther}}| = \frac{k}{(\tilde{\rho} c_p) \times (4/\Delta^2_{\min})} \tag{37}$$

where $\Delta_{\min}$ is the smallest space step.

In unstructured meshes, using the proposed matrix-free method, $\mathbf{S}$ is not symmetric; however, with the time-marching method of [12], the explicit marching of (34) is equally stable. The resulting time step, Δt_m, is the same as that used in a conventional explicit time marching of Maxwell's equations, such as the Courant–Friedrichs–Lewy condition. It satisfies

$$\Delta t_m < \frac{2}{\sqrt{|\xi|_{\max}}} \tag{38}$$

where $|\xi|_{\max}$ is the maximum magnitude of the eigenvalues of $\mathbf{S}$, which is proportional to the inverse of the square of the smallest space step. For the examples simulated in this paper, it is found that Δt_t is much larger than Δt_m. Hence, the thermal equation can be simulated using a much larger step, and the conductivity σ in between the two time instants of the thermal equation is interpolated to obtain that at the time instants for solving Maxwell's equations. Linear interpolation is used in this paper.

In summary, the coupled electrical–thermal system of equations shown in (24)–(26) is discretized in time as (34) and (35), where (34) is marched on in time with the matrix-free explicit marching scheme, as shown in [12], and (35) is marched on in time by a forward difference. The procedure of the cosimulation algorithm is shown in Fig. 2. The electrical and thermal analyses are coupled through the temperature-dependent material properties. When two different time steps are used, within one step of a thermal simulation, there exist ratio $= \Delta t_t / \Delta t_m$ steps of electrical simulations, and n_{total} represents the predefined maximum number of simulation steps.

IV. Numerical Results

In this section, we first validate the proposed method in performing a thermal simulation as well as an electrical–thermal cosimulation. We then apply the proposed method to solve a number of coupled electrical–thermal problems in a variety of structures and meshes. Both FDTD and the time-domain FEM (TDFEM) are used as the reference methods for comparison.

The conductivity σ_0 of copper is 5.8×10^7 S/m. The heat conduction parameters for copper are $k = 398$ W/(m · K), $c_p = 386$ J(kg · K), $\tilde{\rho} = 8930$ kg/m^3, and $\alpha = 0.0039$. All these simulations are conducted with Intel Xeon CPU E5-2690 v2 @ 3.00 GHz having 128-GB memory.

A. Thermal Analysis: Node Basis and Vector Basis

First, we examine the correctness of the proposed matrix-free method for thermal analysis, which involves a vectorization of a scalar thermal equation. Three methods, node basis-based finite-difference method, node basis based FEM method, and vector-based FDTD method, are used as references. In this example, we consider a piece of copper plane whose side length is 0.3 m. The temperature on one side of the plane is 200 °C while being 100 °C on other sides. In Fig. 3(a), we plot the temperature distribution across the whole plane at the steady state. In Fig. 3(b), the temperatures generated from the proposed method and the three reference methods at point (0.2443, 0.2443) m are plotted versus time. Clearly, the temperature at this point gradually grows and finally reaches its expected steady-state value. The results from four different methods are on top of each other, validating the correctness of the proposed vectorization of the thermal equation and its matrix-free solution.

B. Thermal Analysis in a Tetrahedral Mesh

We then simulate a heat conduction problem, which only requires solving the thermal equation. A copper conductor of size $1 \times 0.5 \times 0.75$ m^3 is considered. It is discretized into a tetrahedral mesh, which is shown in Fig. 4. The temperature on the outermost boundary of the cube is set to be 100 °C. To guarantee the stability of the proposed method, we choose a time step of $\Delta t = 0.8$ s.

In Fig. 5(a), the temperature at the point (0.4747, 0.2197, 0.6826) m is plotted versus time. Clearly, the temperature at this point gradually grows and finally reaches its expected steady-state value of 100 °C. It is also shown to agree well with the temperature obtained from the TDFEM. In Fig. 5(b), we plot the entire solution error as compared with the TDFEM, which is shown to be 2.78% when the temperature reaches the steady state. This error is measured by $\|\{T\} - \{T\}_{\text{ref}}\| / \|\{T\}_{\text{ref}}\|$, where $\{T\}$ contains the temperatures of all cells simulated from the proposed method, and $\{T\}_{\text{ref}}$ is the reference solution from the TDFEM. As can be seen from Fig. 5(b), the proposed method is accurate for solving the thermal diffusion equation in an unstructured tetrahedral mesh. The larger difference at the early time is due to a sudden jump from zero to nonzero in the source setup, the high-frequency

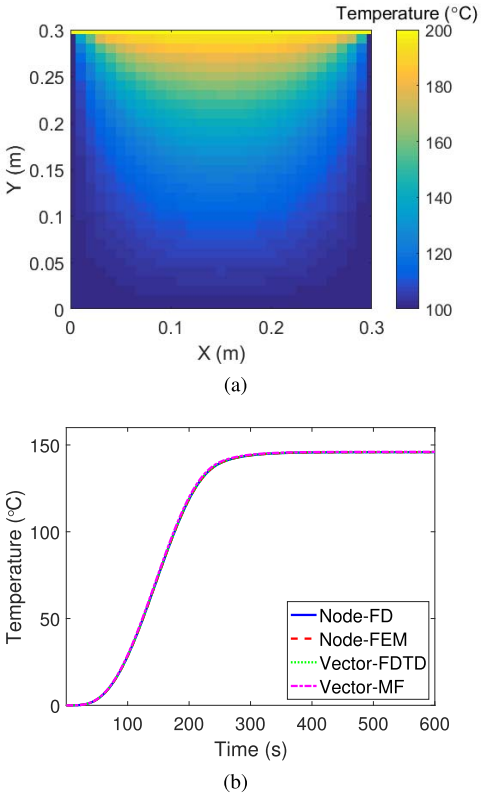

Fig. 3. (a) Temperature distribution at steady state. (b) Transient temperature at an observation point with four different methods.

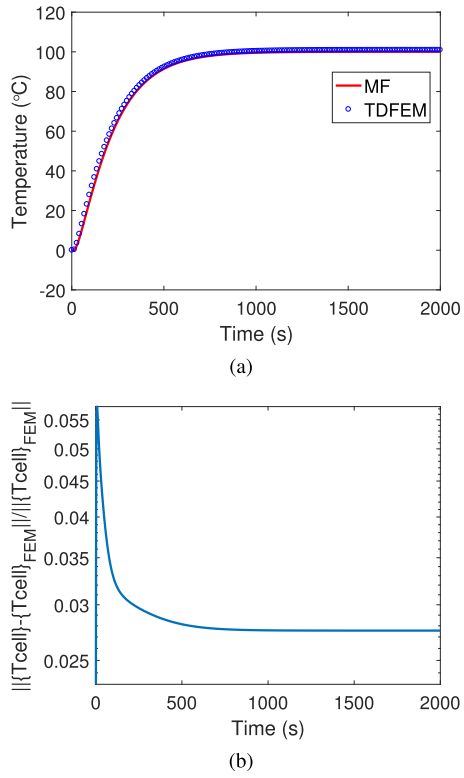

Fig. 5. (a) Transient temperature at one observation point. (b) Entire solution error of the transient temperature at *all* points.

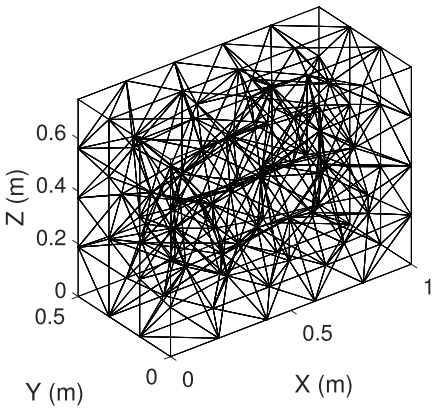

Fig. 4. 3-D tetrahedron discretization of a copper conductor.

components of which are captured by numerical methods in a different way. We also compare the computational efficiency of the proposed method with the TDFEM whose discretization results in a similar number of unknowns. It is shown that the proposed method takes 0.53 s to finish the whole simulation, whereas the TDFEM costs 1.24 s.

C. Electrical–Thermal Cosimulation of Copper Cube in Tetrahedral Mesh

Next, we validate the proposed cosimulation method using the same copper conductor shown in Fig. 4. The conductor is excited by a current source, whose waveform is $2 \times 10^4 (t - t_0)\exp(-(t - t_0)^2/\tau^2)$, with $\tau = 6.0 \times 10^{-9}$ s and $t_0 = 4\tau$. The time step used in the Maxwell part of the cosimulation is $\Delta t_m = 2.4 \times 10^{-11}$ s, while that in the thermal part is $\Delta t_t = 2.4 \times 10^{-9}$ s $= 100\Delta t_m$. The temperature on the outermost boundary of the cube is set to be 0 °C. The simulated temperatures in all of the tetrahedral elements are plotted versus time in Fig. 6(a). The relative error of these temperatures, measured by $\|\{T\} - \{T\}_{\text{ref}}\|/\|\{T\}_{\text{ref}}\|$, is plotted in Fig. 6(b), where $\{T\}$ contains the temperatures of all elements simulated from the proposed method, and $\{T\}_{\text{ref}}$ is the reference TDFEM solution. Good accuracy is observed across the entire window. In Fig. 7(a), we plot the electric field at an observation point (0.1971, 0.0556, 0.0662) m obtained from the cosimulation in comparison with the result obtained from a Maxwell-only simulation. It is clear that the thermal effect is observable in this example, and the cosimulation is able to capture the combined electrical–thermal effects. We also plot the TDFEM results in Fig. 7. Excellent agreement is observed between the TDFEM and the proposed method. Furthermore, we have compared the entire electric field solution with those of the TDFEM, by evaluating the total error of $\|\{e\} - \{e\}_{\text{ref}}\|/\|\{e\}_{\text{ref}}\|$. $\{e\}$ containing all e_i unknowns is from the proposed method, and $\{e\}_{\text{ref}}$ is from the TDFEM solution. The error is shown in Fig. 7(b) as a function of time, validating the accuracy of the proposed method for electrical–thermal cosimulation. Again, to demonstrate the efficiency of the proposed method, we compare our matrix-free method with the TDFEM method. In the cosimulation, TDFEM needs to do LU factorization at each time when the material properties are updated, while the proposed method

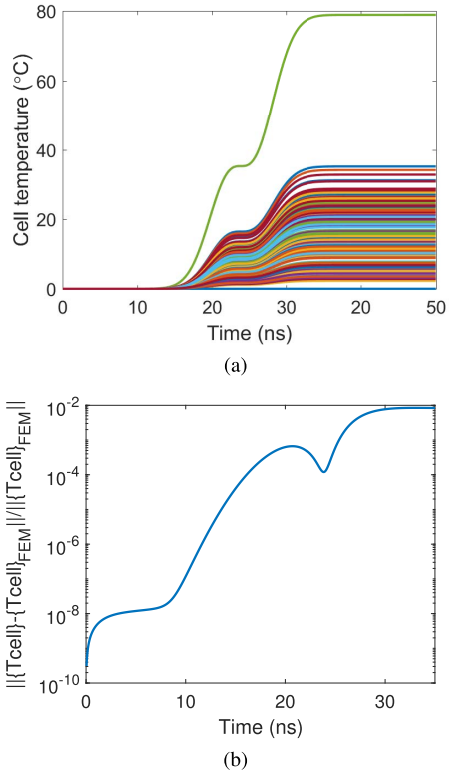

Fig. 6. Copper cube cosimulation. (a) Temperature versus time at all points. (b) Entire T solution error as a function of time.

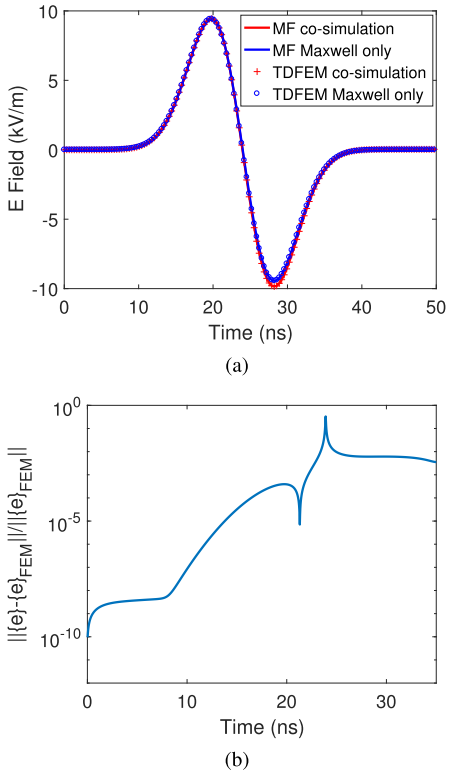

Fig. 7. Copper cube cosimulation. (a) Simulated electric field at one point. (b) Entire **E**-field solution error as a function of time.

has no factorization cost since it is free of matrix solution. In contrast to the 81.39 s cost by TDFEM, the proposed method only takes 6.85 s to finish the whole simulation.

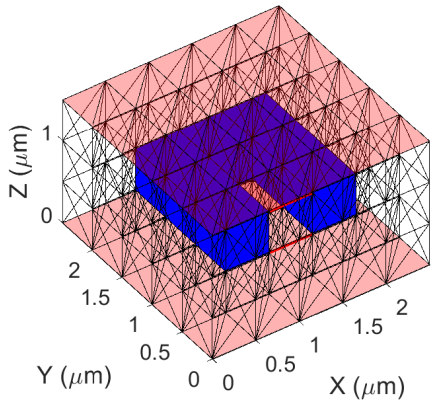

Fig. 8. 3-D view of a u-type resistor.

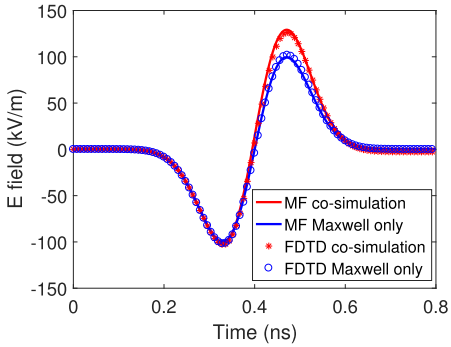

Fig. 9. U-type conductor electrical–thermal cosimulation: electric field at an observation point.

D. U-Type Conductor Discretized Into Tetrahedral Elements

A 3-D u-type resistor is discretized into tetrahedral elements, as shown in Fig. 8. These tetrahedral elements are generated from brick elements so that FDTD can be used for comparison. σ_0 of all metal is 5.8×10^7 S/m, and the surrounding material has a relative permittivity of 4. The two ends of the conductor are excited by a current source, which is shown by the red line in Fig. 8. The boundary conditions are perfect magnetic conductor (PMC) on the left, right, front, and back sides and perfect electric conductor (PEC) on the top and at the bottom, with the temperature set to be 0 °C. The source waveform is a Gaussian derivative pulse of $5.7 \times 10^3 (t - t_0) \exp(-(t - t_0)^2/\tau^2)$, with $\tau = 1 \times 10^{-10}$ s and $t_0 = 4\tau$. In Fig. 9, we plot the electric field at the point (0.5, 0.75, 0.5) μm along the y-direction edge in the conductor obtained with the Maxwell-thermal cosimulation versus that from a Maxwell-only simulation. With a peak cell temperature of 82.17 °C, the thermal effect on electrical performance can be clearly observed. For validation purpose, the electric field simulated at the same point along the same direction from the FDTD method is also plotted in Fig. 9. Good agreement is observed.

E. Electrical–Thermal Cosimulation of Coaxial Cylinder in Prism Mesh

We have examined the capability of the proposed method in handling irregular prism meshes as well. This example has

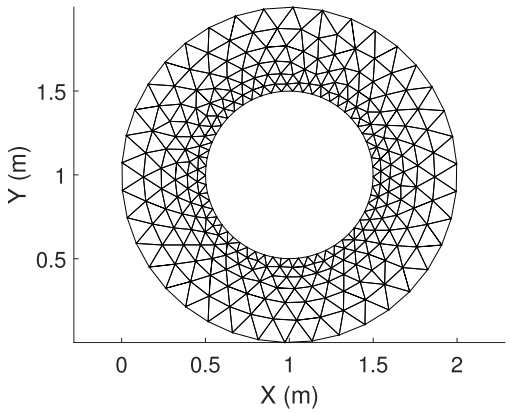

Fig. 10. Top view of the triangular prism mesh of a coaxial cylinder structure.

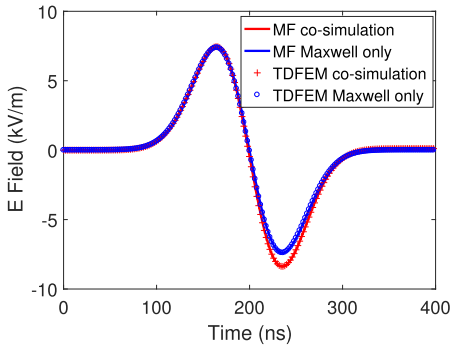

Fig. 11. Coaxial cylinder cosimulation: simulated electric field at one point.

an irregular triangular prism mesh, the top view of which is shown in Fig. 10. The structure has two layers of triangular prism elements (into this paper) with each layer being 0.05 m thick. The discretization results in 3092 edges and 1038 triangular prisms. The conductor is excited by a current source, whose waveform is $2.5 \times 10^4(t-t_0)\exp(-(t-t_0)^2/\tau^2)$, with $\tau = 5.0 \times 10^{-8}$ s and $t_0 = 4\tau$. The temperature on both the innermost boundary and the outermost boundary is set to be 0 °C. The time step used in both the Maxwell part and the thermal part of the cosimulation is $\Delta t_m = 2.0 \times 10^{-10}$ s. In Fig. 11(a), we plot the electric field at an observation point (0.1845, 0.7067, 0.0250) m obtained from the cosimulation in comparison with the result obtained from a Maxwell-only simulation. The thermal effect is clearly observable in this example, and the cosimulation is able to capture the combined electrical–thermal effects. We also plot the TDFEM results in Fig. 11. Excellent agreement is observed between the TDFEM and the proposed method.

F. Lossy Package Inductor With Triangular Prism Elements

In this example, we simulate a package inductor made of lossy conductors of initial conductivity 5.8×10^7 S/m, which is embedded in a dielectric material of relative permittivity 3.4. Its geometry and material parameters are shown in Fig. 12. The inductor is discretized into layers of triangular prism elements. The top view of the mesh is shown in Fig. 13. The boundary conditions are PMC on the left, right, front, and back sides, and PEC on the top and at the bottom, with the temperature set to be 0 °C. A current source is launched at one end of the inductor, which is marked with blue color. The source waveform is a Gaussian derivative pulse of $0.5 \times 10^4(t-t_0)\exp(-(t-t_0)^2/\tau^2)$, with $\tau = 0.5 \times 10^{-10}$ s and $t_0 = 4\tau$. In Fig. 14, we plot the electric field along the z-direction at the point $(-600, -25, 37.5)$ μm in the inductor obtained with the Maxwell-thermal cosimulation versus that from a Maxwell-only simulation. With a peak cell temperature of 51.3 °C, the thermal effect on electrical performance can be clearly observed. For validation purpose, the electric field simulated from the TDFEM is also plotted for comparison. Good agreement is observed.

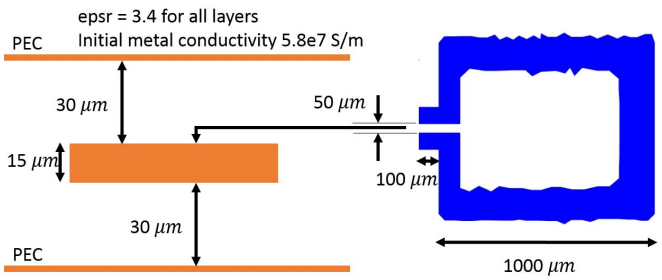

Fig. 12. Illustration of materials and geometry of a package inductor.

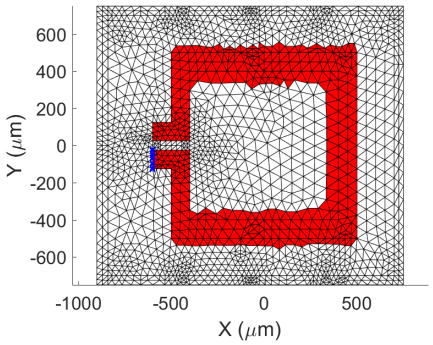

Fig. 13. Top view of the triangular prism element mesh.

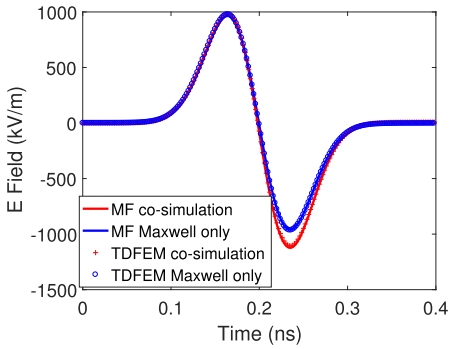

Fig. 14. Package inductor electrical–thermal cosimulation: electric field at an observation point.

G. 3-D On-Chip Power Grid Discretized Into Tetrahedral Mesh

Next, we simulate a 3-D on-chip power grid, as shown in Fig. 15(a) and (b). The power grid is discretized into

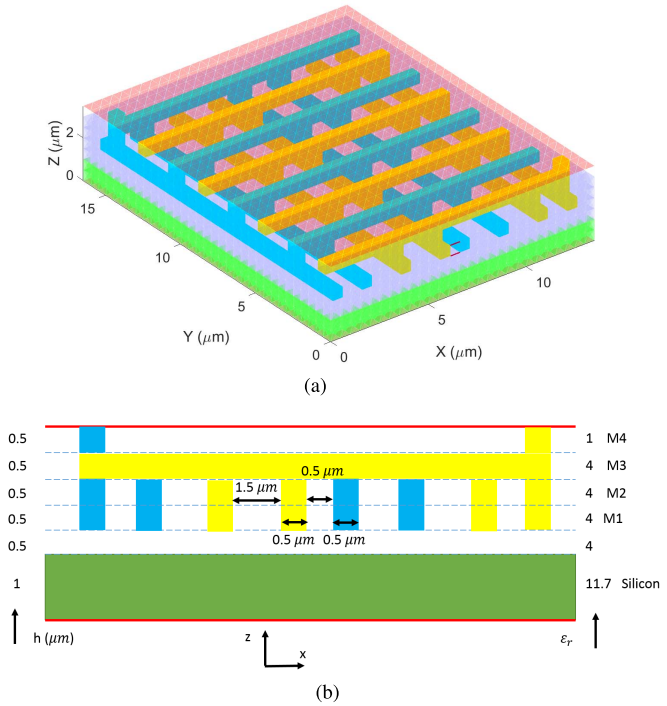

Fig. 15. (a) 3-D view of an on-chip power grid. (b) Geometry and cross-sectional view.

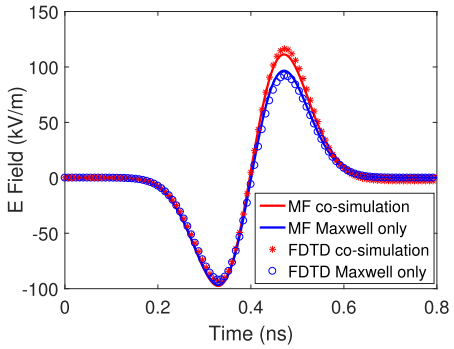

Fig. 16. Power grid electrical–thermal cosimulation: electric field at an observation point.

a tetrahedral mesh to model nonuniform materials and process variations with fewer unknowns. σ_0 of all metal is 5.8×10^7 S/m, and that of the silicon substrate is 10^4 S/m. The boundary conditions are PMC on the left, right, front, and back sides, and PEC on the top and at the bottom, with the temperature set to be 0 °C. The near end between a pair of power and ground wires in layer M1 is excited by a current source, which is shown by the red line in Fig. 15. The source waveform is a Gaussian derivative pulse of $3.8 \times 10^3 (t - t_0)\exp(-(t - t_0)^2/\tau^2)$, with $\tau = 1 \times 10^{-10}$ s and $t_0 = 4\tau$. In Fig. 16, we plot the electric field along the y-direction at the point (6, 0.75, 1.5) μm in the M1 layer obtained with the Maxwell-thermal cosimulation versus that from a Maxwell-only simulation. TDFEM results are also shown for comparison. With a peak cell temperature of 78.84 °C, the thermal effect on electrical performance can be clearly observed. If using TDFEM to handle the same tetrahedral mesh and using the same time step for the Maxwell and thermal simulations, the TDFEM costs 47.1 s per time step, while the proposed method costs 0.29 s only. If using two different time steps for Maxwell and thermal simulations and only update conductivity at thermal time step, the CPU time cost at one thermal time step, which includes one thermal simulation and 100 steps of Maxwell's simulations, is 12.17 s for the proposed method and 102.54 s for the TDFEM, demonstrating the efficiency of the proposed method.

V. Conclusion

In this paper, we develop a matrix-free algorithm for solving the coupled full-wave Maxwell's equations and the thermal diffusion equation in the time domain. The thermal equation is vectorized to develop a matrix-free solution without increasing the problem size. The matrix-free property is achieved regardless of the element shape used for discretizing Maxwell's or thermal equations. The stability of the coupled nonlinear system of equations is also analyzed in detail and found to be ensured with a correct choice of time step in explicit time marching. Numerical experiments have demonstrated the accuracy and efficiency of the proposed matrix-free method for simulating thermal as well as coupled electrical–thermal problems. The proposed method can also be extended to achieve an arbitrary higher order of accuracy in both space and time.

References

[1] D. Jiao and J. Jin, "Finite element analysis in time domain," in *The Finite Element Method in Electromagnetics*. Hoboken, NJ, USA: Wiley, 2002, pp. 529–584.

[2] M. Feliziani and F. Maradei, "Hybrid finite element solutions of time dependent Maxwell's curl equations," *IEEE Trans. Magn.*, vol. 31, no. 3, pp. 1330–1335, May 1995.

[3] K. Yee, "Numerical solution of initial boundary value problems involving Maxwell's equations in isotropic media," *IEEE Trans. Antennas Propag.*, vol. AP-14, no. 3, pp. 302–307, May 1966.

[4] A. Taflove and S. C. Hagness, *Computational Electrodynamics: The Finite-Difference Time-Domain Method*. Boston, MA, USA: Artech House, 2000.

[5] D. Mavriplis, "On convergence acceleration techniques for unstructured meshes," in *Proc. 29th AIAA Fluid Dyn. Conf.*, 1998, p. 2966.

[6] S. D. Gedney and J. A. Roden, "Numerical stability of nonorthogonal FDTD methods," *IEEE Trans. Antennas Propag.*, vol. 48, no. 2, pp. 231–239, Feb. 2000.

[7] M. Cinalli and A. Schiavoni, "A stable and consistent generalization of the FDTD technique to nonorthogonal unstructured grids," *IEEE Trans. Antennas Propag.*, vol. 54, no. 5, pp. 1503–1512, May 2006.

[8] H.-X. Zheng and K. W. Leung, "A nonorthogonal ADI-FDTD algorithm for solving two dimensional scattering problems," *IEEE Trans. Antennas Propag.*, vol. 57, no. 12, pp. 3891–3902, Dec. 2009.

[9] M. M. Rana and A. S. Mohan, "Nonorthogonal LOD-FDTD method for EM scattering from two-dimensional structures," *IEEE Trans. Electromagn. Compat.*, vol. 55, no. 4, pp. 764–772, Aug. 2013.

[10] R. T. Lee, J. G. Maloney, B. N. Baker, and D. W. Landgren, "FDTD in curvilinear coordinates using a rectangular FDTD formulation," in *Proc. IEEE Int. Symp. Antennas Propag.*, Jul. 2011, pp. 2326–2329.

[11] L. Bernard and L. Pichon, "Generalized finite difference scheme using mainly orthogonal and locally barycentric dual mesh for electromagnetic problems," *Eur. Phys. J. Appl. Phys.*, vol. 52, no. 2, Art. no. 23307, 2010.

[12] J. Yan and D. Jiao, "Accurate and stable matrix-free time-domain method in 3-D unstructured meshes for general electromagnetic analysis," *IEEE Trans. Microw. Theory Techn.*, vol. 63, no. 12, pp. 4201–4214, Dec. 2015.

[13] J. Yan and D. Jiao, "Matrix-free time-domain method for general electromagnetic analysis in 3-d unstructured meshes–modified-basis formulation," *IEEE Trans. Microw. Theory Techn.*, vol. 64, no. 8, pp. 2371–2382, Aug. 2016.

[14] J. Yan and D. Jiao, "Time-domain method having a naturally diagonal mass matrix independent of element shape for general electromagnetic analysis—2-D formulations," *IEEE Trans. Antennas Propag.*, vol. 65, no. 3, pp. 1202–1214, Mar. 2017.
[15] T. Lu and J.-M. Jin, "Electrical-thermal co-simulation for analysis of high-power RF/microwave components," *IEEE Trans. Electromagn. Compat.*, vol. 59, no. 1, pp. 93–102, Feb. 2017.
[16] N. Li, J. Mao, W.-S. Zhao, M. Tang, W. Chen, and W.-Y. Yin, "Electrothermal cosimulation of 3-D carbon-based heterogeneous interconnects," *IEEE Trans. Compon., Packag., Manuf. Technol.*, vol. 6, no. 4, pp. 518–526, Apr. 2016.
[17] X. Zhang, Z. Chen, and Y. Yu, "An unconditional stable meshless ADI-RPIM for simulation of coupled transient electrothermal problems," *IEEE J. Multiscale Multiphys. Comput. Tech.*, vol. 1, pp. 98–106, Nov. 2016.
[18] Y. Nakatani, T. Sekine, and H. Asai, "Three-dimensional iterative electrical-thermal co-simulation (3-D IETC) method for power/thermal integrity analysis," in *Proc. IEEE CPMT Symp. Jpn. (ICSJ)*, Kyoto, Japan, Nov. 2016, pp. 167–168.
[19] T. Casper *et al.*, "Electrothermal simulation of bonding wire degradation under uncertain geometries," in *Proc. Design, Automat. Test Eur. Conf. Exhib. (DATE)*, Mar. 2016, pp. 1297–1302.
[20] A. Leggieri, D. Passi, F. D. Paolo, B. Spataro, and E. Dyunin, "Design of a sub-millimetric electron gun with analysis of thermomechanical effects on beam dynamics," *Vacuum*, vol. 122, pp. 103–116, Dec. 2015.
[21] J. Xie and M. Swaminathan, "Electrical–thermal cosimulation with nonconformal domain decomposition method for multiscale 3-D integrated systems," *IEEE Trans. Compon., Packag., Manuf. Technol.*, vol. 4, no. 4, pp. 588–601, Apr. 2014.
[22] F. Torres and B. Jecko, "Complete FDTD analysis of microwave heating processes in frequency-dependent and temperature-dependent media," *IEEE Trans. Microw. Theory Techn.*, vol. 45, no. 1, pp. 108–117, Jan. 1997.
[23] K. Zeng and D. Jiao, "Matrix-free method for Maxwell-thermal co-simulation in unstructured meshes," in *IEEE MTT-S Int. Microw. Symp. Dig.*, Jun. 2018, pp. 201–204.
[24] E. C. Young, *Vector and Tensor Analysis*. New York, NY, USA: Dekker, 1973.
[25] G. Teschl, *Ordinary Differential Equations and Dynamical Systems*. Providence, RI, USA: Amer. Math. Soc., 2012.

Kaiyuan Zeng (GS'18) received the B.S. degree in electronic engineering and information science from the University of Science and Technology of China, Hefei, China, in 2012. He is currently pursuing the Ph.D. degree in electrical engineering at the On-Chip Electromagnetics Group, Purdue University, West Lafayette, IN, USA.

His current research interests include computational electromagnetics and multiphysics modeling.

Mr. Zeng was a recipient of the Honorable Mention Award from the IEEE International Symposium on Antennas and Propagation in 2018 and the Best Student Paper Award from the IEEE Wireless and Microwave Technology Conference in 2015.

Dan Jiao (M'02–SM'06–F'16) received the Ph.D. degree in electrical engineering from the University of Illinois at Urbana–Champaign, Urbana, IL, USA, in 2001.

She was with the Technology Computer-Aided Design (CAD) Division, Intel Corporation, Santa Clara, CA, USA, until 2005, as a Senior CAD Engineer, a Staff Engineer, and a Senior Staff Engineer. In 2005, she joined the School of Electrical and Computer Engineering, Purdue University, West Lafayette, IN, USA, as an Assistant Professor, where she is currently a Professor. She has authored three book chapters and over 260 papers in refereed journals and international conferences. Her current research interests include computational electromagnetics, high-frequency digital, analog, mixed-signal, and RF integrated circuit design and analysis, high-performance VLSI CAD, modeling of microscale and nanoscale circuits, applied electromagnetics, fast and high-capacity numerical methods, fast time-domain analysis, scattering and antenna analysis, RF, microwave, and millimeter-wave circuits, wireless communication, and bioelectromagnetics.

Dr. Jiao was a recipient of the 2010 Ruth and Joel Spira Outstanding Teaching Award, the 2008 National Science Foundation CAREER Award, the 2006 Jack and Cathie Kozik Faculty Startup Award (which recognizes as an outstanding new faculty member of the School of Electrical and Computer Engineering, Purdue University), the 2006 Office of Naval Research Award under the Young Investigator Program, the 2004 Best Paper Award presented at the Intel Corporation's Annual Corporate-Wide Technology Conference (Design and Test Technology Conference) for her work on generic broadband model of high-speed circuits, the 2003 Intel Corporation's Logic Technology Development (Ltd.) Divisional Achievement Award, the Intel Corporation's Technology CAD Divisional Achievement Award, the 2002 Intel Corporation's Components Research the Intel Hero Award (Intel-wide she was a 10th recipient), the Intel Corporation's Ltd. Team Quality Award, and the 2000 Raj Mittra Outstanding Research Award presented by the University of Illinois at Urbana–Champaign. She received the 2013 S. A. Schelkunoff Prize Paper Award from the IEEE Antennas and Propagation Society, which recognizes as the Best Paper published in the IEEE TRANSACTIONS ON ANTENNAS AND PROPAGATION during the previous year. She was among the 21 women faculty selected across the country as the 2014–2015 Fellow of Executive Leadership in Academic Technology and Engineering at Drexel, a national leadership program for women in the academic STEM fields. She has been named a University Faculty Scholar by Purdue University since 2013. She was among the 85 engineers selected throughout the nation for the National Academy of Engineering's 2011 U.S. Frontiers of Engineering Symposium. She has served as the Reviewer for many IEEE journals and conferences. She is an Associate Editor of the IEEE TRANSACTIONS ON COMPONENTS, PACKAGING, AND MANUFACTURING TECHNOLOGY.